Characterization of Metal Binding in the Active Sites of Acireductone Dioxygenase Isoforms from *Klebsiella* ATCC 8724[†]

Sergio C. Chai,[‡,§] Tingting Ju,[⊥,||] Marina Dang,[⊥] Rachel Beaulieu Goldsmith,[#] Michael J. Maroney,[‡] and Thomas C. Pochapsky*,[⊥,#,▽]

Department of Chemistry, University of Massachusetts, Amherst, Massachusetts 01003, and Departments of Chemistry and Biochemistry and Rosenstiel Basic Medical Sciences Institute, MS 015, Brandeis University, Waltham, Massachusetts 02454

Received March 1, 2007; Revised Manuscript Received December 20, 2007

ABSTRACT: The two acireductone dioxygenase (ARD) isozymes from the methionine salvage pathway of *Klebsiella* ATCC 8724 present an unusual case in which two enzymes with different structures and distinct activities toward their common substrates (1,2-dihydroxy-3-oxo-5-(methylthio)pent-1-ene and dioxygen) are derived from the same polypeptide chain. Structural and functional differences between the two isozymes are determined by the type of M^{2+} metal ion bound in the active site. The Ni^{2+}-bound NiARD catalyzes an off-pathway shunt from the methionine salvage pathway leading to the production of formate, methylthiopropionate, and carbon monoxide, while the Fe^{2+}-bound FeARD′ catalyzes the on-pathway formation of methionine precursor 2-keto-4-methylthiobutyrate and formate. Four potential protein-based metal ligands were identified by sequence homology and structural considerations. Based on the results of site-directed mutagenesis experiments, X-ray absorption spectroscopy (XAS), and isothermal calorimetry measurements, it is concluded that the same four residues, His96, His98, Glu102 and His140, provide the protein-based ligands for the metal in both the Ni- and Fe-containing forms of the enzyme, and subtle differences in the local backbone conformations trigger the observed structural and functional differences between the FeARD′ and NiARD isozymes. Furthermore, both forms of the enzyme bind their respective metals with pseudo-octahedral geometry, and both may lose a histidine ligand upon binding of substrate under anaerobic conditions. However, mutations at two conserved nonligand acidic residues, Glu95 and Glu100, result in low metal contents for the mutant proteins as isolated, suggesting that some of the conserved charged residues may aid in transfer of metal from *in vivo* sources or prevent the loss of metal to stronger chelators. The Glu100 mutant reconstitutes readily but has low activity. Mutation of Asp101 results in an active enzyme that incorporates metal *in vivo* but shows evidence of mixed forms.

The methionine salvage pathway (MSP) plays a critical role in regulating a number of important metabolites in prokaryotes and eukaryotes. The first committed intermediate in the MSP, methylthioadenosine (MTA),[1] is formed from *S*-adenosylmethionine (SAM, AdoMet) as a biproduct of polyamine biosynthesis. MTA is a potent inhibitor of polyamine biosynthesis and transmethylation reactions (*1*). In turn, polyamines are important in the regulation of the cell cycle, being required for cell growth and proliferation. Inhibition of polyamine biosynthesis arrests DNA replication and perturbs cell cycle progression (*2*), whereas elevated polyamine levels are often associated with tumor formation (*3*, *4*). The concentration of MTA is tightly regulated via the MSP, whereby MTA is recycled through a series of reactions that return the γ-thiomethyl group of MTA to methionine (*5*). The penultimate intermediate in this cycle is 1,2-dihydroxy-3-keto-5-methylthiopentene, an acireductone.

In the bacterium *Klebsiella* ATCC strain 8724, two enzymes have been identified that catalyze the oxidation of acireductone by dioxygen (*6*). Both of these enzymes are known as acireductone dioxygenases (ARDs) (*7*). FeARD′

[†] This work was supported in part by USPHS Grant R01-GM067786 (T.C.P.). Acknowledgment is made to the donors of The American Chemical Society Petroleum Research Fund for partial support (M.J.M.). Trainee funding (S.C.C.) was provided by the NIH-Chemistry Biology Interface Program, Grant T32-GM08515. XAS data collection at the National Synchrotron Light Source at Brookhaven National Laboratory was supported by the U.S. Department of Energy, Division of Materials Sciences and Division of Chemical Sciences. Beamline X9B at NSLS is supported in part by the NIH.

* To whom correspondence should be addressed. E-mail: pochapsk@brandeis.edu. Phone: 781-736-2559. Fax: 781-736-2516.

[‡] University of Massachusetts.

[§] Current address: Department of Biochemistry and Molecular Biology, Indiana University School of Medicine, 635 Barnhill Dr., Room 1007, Indianapolis Indiana 46202.

[⊥] Department of Chemistry, Brandeis University.

[||] Current address: Department of Molecular Pharmacology, Physiology and Biotechnology, Brown University, 70 Ship Street, GE3, Providence, Rhode Island 02912.

[#] Department of Biochemistry, Brandeis University.

[▽] Rosenstiel Basic Medical Sciences Institute, Brandeis University.

[1] Abbreviations: ARD, acireductone dioxygenase; ATCC, American Type Culture Collection; DEAE, diethylaminoethylcellulose; DTT, dithiothreotol; EDTA, ethylenediaminetetraacetic acid; EXAFS, extended X-ray absorbance fine structure; FPLC, fast protein liquid chromatography; GF-AAS, graphite furnace atomic absorption spectroscopy; IPTG, isopropyl-β-D-1-thiogalactopyranoside; ITC, isothermal calorimetry; MOPS, 3-morpholinopropanesulfonic acid; MTA, methylthioadenosine; NMR, nuclear magnetic resonance; SAM, *S*-adenosylmethionine; SDS−PAGE, sodium dodecylsulfate−polyacrylamide gel electrophoresis; XAS, X-ray absorption spectroscopy.

10.1021/bi7004152 CCC: $40.75
Published on Web 02/01/2008

converts acireductone to formate and the keto-acid precursor of methionine, 2-keto-4-methylthiobutyrate, whereas acireductone is shunted off-pathway by NiARD to produce 3-methylthiopropionate, carbon monoxide, and formate (*6*−*8*). This off-pathway shunt has also been observed in *Bacillus subtilis* (*9*) and *Escherichia coli* (*10*). Both FeARD′ and NiARD occur naturally in *Klebsiella* (*10*), and both are obtained upon overexpression of a single open reading frame in *E. coli*. Their apoproteins are identical 179-amino acid residue polypeptides with a mass of 20.2 kDa, and the activities of the two enzymes are interconverted by exchanging Fe^{2+} and Ni^{2+} (*7*). Both enzymes are monomeric and coelute from a size-exclusion column but can be separated by ion-exchange and hydrophobic interaction chromatography. FeARD′ and NiARD represent the only known pair of naturally occurring metalloenzymes with distinct chemical and physical properties determined solely by metal ion content.

Both FeARD′ and NiARD are members of the structural superfamily known as cupins (*11*). A model for the solution structure of NiARD was determined by multidimensional NMR methods (*12*), and a refinement of that structure was recently described (*13*). X-ray absorption spectroscopy (XAS) studies of the structure of the catalytic Ni center in resting NiARD enzyme and the enzyme−substrate (ES) complex have been reported (*14*). We have also described a structural model for FeARD′ and identified a structural entropy switch that interconverts the two isoforms (*15*) (Figure 1).

For both the Fe- and Ni-containing isozymes, the paramagnetism of the bound metal complicates the determination of the structure of the active site by NMR methods. For NiARD, the original modeled structure of the active site was based on homology with jack bean canavalin (*12*, *16*) and upon refinement, with the recently published crystallographic structure of the house mouse homologue of ARD, *Mm*ARD (*13*, *17*) (Figure 1). In both cases, the results of XAS studies of NiARD were used to determine Ni-ligand bond lengths and coordination geometry (*14*). The recently published FeARD′ structural model is based on the structure of a stable soluble metal-free mutant of *Klebsiella* ARD, H98S ARD, after the serendipitous discovery that this mutant is isostructural with FeARD′ as determined by multidimensional NMR experiments (*15*). As with NiARD, Fe-ligand bond lengths and ligation geometry was established using the results of XAS experiments that are detailed here.

Based on the evidence of XAS, site-directed mutagenesis, and isothermal calorimetry experiments described in this paper as well as evidence from other laboratories and our own previous work (*14*, *18*), we conclude that the same amino acid residues, His96, His98, Glu102, and His140 provide the protein-based ligands for the metal in both Fe- and Ni-bound forms of ARD and that both metals are bound in approximately octahedral geometry with solvent-derived ligands providing the remainder of the coordination sphere. This conclusion implies that relatively subtle differences between the two metal−protein complexes are amplified by the surrounding protein structure, giving two enzymes of different structures and activities from a single polypeptide.

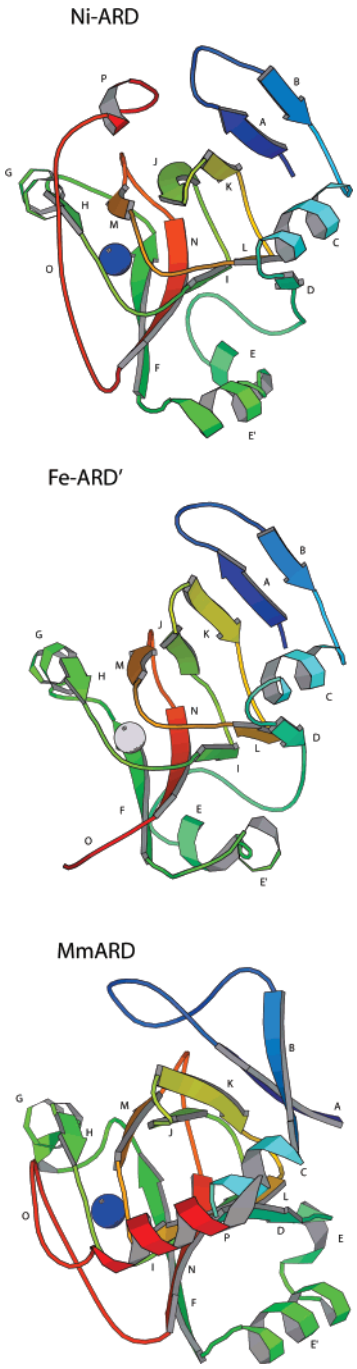

FIGURE 1: Solution structures of NiARD (PDB entry 1ZRR) and FeARD′ (PDB entry 2HJI) from *Klebsiella* and crystallographic structure of *Mm*ARD from *Mus musculus* (PDB entry 1VR3). Letters reference to the *Klebsiella* ARD sequence as follows: A (Ala2−Phe6), B (Leu15−Ser18), C (Glu23−Lys31), D (Val33−Glu36), E (Thr52−Tyr57), E′ (Ile61−Lys68), F (Ser72−Leu78), G (Lys85−Glu90), H (Phe92−Glu95), I (Arg104−Val107), J (Gly111−Ile117), K (Glu120−Leu125), L (Asn129−Ile132), M (His140−Met144), N (Phe150−Phe156), O (Trp162−Phe166), P (Ile171−Ala174). Features in the *Mm*ARD structure are lettered to show correspondence with the *Klebsiella* ARD structures. Blue spheres show position of Ni^{2+} in NiARD and unknown metal in *Mm*ARD; gray sphere shows position of Fe^{2+} in FeARD′. Figures were generated using Molscript (*35*).

MATERIALS AND METHODS

Site-Directed Mutagenesis, Expression and Characterization of ARD Mutants. Mutations of proposed metal binding ligands and conserved acidic residues in the ARD active site

were generated using the Quik-Change kit and protocol (Stratagene, La Jolla, CA). All primers for mutagenesis were designed in-house and obtained in purified form from Operon Biotechnologies, Inc. (Huntsville, AL). The WT ARD gene in a pET3a vector was used as template (*19*), and all of the mutant genes were also placed in pET3a expression vectors for amplification and expression. Mutant constructs were amplified in XL1-Blue *E. coli* (Stratagene), plasmids from selected colonies were then mini-prepped (Promega, Madison, WI), and the presence of the mutations was confirmed by complete sequencing of the mutant gene using standard methods (Brandeis University Biotechnology Center).

For protein expression, a pET3a vector containing the appropriate mutant or WT ARD construct was transformed into *E. coli* strain BL21(DE3) and grown in 5 mL of Luria−Bertani (LB) broth containing 50 mg/L ampicillin. For production of wild type and mutant proteins, 1 mL of the inoculum culture was transferred to 1 L of sterile LB medium containing 50 mg/L ampicillin. Protein expression was induced when the culture reached a cell density OD_{600} between 0.5 and 0.6 by the addition of IPTG to a final concentration of 0.5 mM. Cells were harvested by centrifugation 3 h after induction.

Mutant ARD Characterization. Soluble mutant ARD proteins were purified following previously described methods (*19*), and protein purity was determined by SDS−PAGE gel electrophoresis. For those mutants of ARD found in significant quantities in the cytosol, the metal contents of the purified proteins were determined by GF-AAS (Dr. Peter Kerr, Univ. of Massachusetts Amherst). The purified soluble mutants were tested for acireductone dioxygenase activity and compared with WT NiARD and FeARD′ by ^{1}H NMR spectroscopy. E100A and H98S mutants were specifically reconstituted with Ni^{2+} and Fe^{2+} in the course of ITC experiments (vide infra), and the reconstituted proteins were characterized for keto-acid production from acireductone (on-pathway or FeARD′ activity) and CO production (off-pathway or NiARD activity). Coupled activity assays have been described previously for production of keto-acid and formate (*20*). For determination of carbon monoxide production, a gas chromatographic assay was used as described by Sundin (*21*). In this assay, headspace gas samples released by acidification of enzyme assay solutions are injected via gastight syringe onto a polystyrene−divinylbenzene fused silica capillary column (50 m × 0.32 mm, Agilent catalog 19091P-Q04) mounted on a Hewlett-Packard model 6890 gas chromatograph operating at 60 °C. Column effluent is mixed with H_2 and passed through a Ni catalyst chamber, so that CO and CO_2 are hydrogenated to methane, then detected by a flame ionization detector. System control and peak quantitation was performed using the Agilent ChemStation software package. Detector response was calibrated by injection of fixed dilutions of CO gas in N_2.

Reconstitution and Purification of FeARD′. In order to ensure maximum Fe^{2+} occupancy of ARD for XAS experiments, WT ARD was reconstituted as follows. WT ARD was expressed as described above, and the cells were harvested by centrifugation. Four grams of cell paste was suspended in 40 mL of lysis buffer (50 mM Tris-HCl, pH 8.0, 1 mM DTT, 4 mg of DNAase I, 3 mg of RNAase A, 100 mg of lysozyme, and 10 mg of tosyl chloride). The mixture was stirred at 4 °C overnight. All steps up to the chromatography were carried out on ice. The cells were disrupted by sonication (70% output × 30 s × 6 times). Urea (28.8 g) was added while stirring under a stream of argon (Ar) gas to reach a final urea concentration of 8 M. DTT was added to a final concentration of 5 mM. A Ni^{2+}-specific chelator, dimethylglyoxime, was then added to reach a final concentration of 1.4 mM. After stirring under Ar for 10 min, solid $FeSO_4$ was added with stirring to the solution to a final concentration of 10 mM. The solution turned slightly green, indicating a minimum degree of Fe^{3+} formation. After another 10 min, the solution was diluted 8-fold by addition of 420 mL of degassed and Ar-saturated 50 mM Tris-HCl (pH 7.4). The diluted solution was stirred under Ar for an additional 15 min, and then solids were removed by centrifugation (JA-10 rotor, 5000 rpm, 60 min). The cleared supernatant was loaded onto a DEAE anion exchange column pre-equilibrated with buffer A (20 mM Tris, pH 7.4, degassed and Ar-saturated). After unbound proteins were washed from the column by 100 mL of buffer A, a linear gradient of 0−0.5 M NaCl in a total volume of 250 mL was used to elute FeARD′. ARD fractions were identified by SDS−PAGE gel electrophoresis. The ARD fractions were combined and concentrated, then injected in appropriate amounts onto a Superose 6 size exclusion column equilibrated with 50 mM KPi (pH 7.4) buffer and mounted on an AKTA FPLC. Purity of fractions eluted from the column was determined by SDS−PAGE. The purest fractions were combined and concentrated for preparation of XAS samples.

XAS Sample Preparation. Purified resting state FeARD′ was buffer-exchanged via desalting column into 50 mM triethanolaminoacetic acid at pH 7.5 and concentrated to 1 mM using a spin concentrator. Fifty microliters of this solution was loaded into an XAS sample holder and frozen immediately in liquid nitrogen. Due to the relative reactivity of ARD substrate with oxygen, the FeARD′ ES complex must be generated *in situ* anaerobically. The substrate used in this work was a des-thiomethyl form of acireductone, 1,2-dihydroxy-3-oxo-hex-1-ene, produced by the action of E1 enolase-phosphatase on the precursor 1-phosphonooxy-2,2-dihydroxy-3-oxo-hexane (*22*). This substrate shows similar reactivity and product distributions with ARD as the natural substrate (*20*). Sufficient E1 substrate, pH adjusted to 7.5, was mixed with FeARD′ to obtain a 12 mM final concentration of substrate and 1.6 mM final concentration of FeARD′ in 50 mM triethanolaminoacetic acid, pH adjusted with NaOH (pH 7.5). This solution was allowed to deoxygenate overnight in an anaerobic chamber. Deoxygenated E1 enolase-phosphatase and $MgCl_2$ (30 μM and 50 μM final concentrations, respectively) were then added to the ARD−precursor mixture, and the enolase-phosphatase reaction was allowed to proceed for 30 min under anaerobic conditions. The reaction mixture (about 50 μL) was then transferred to the XAS sample holder and immediately frozen in liquid nitrogen.

Preparation of Metal-Free WT and Mutant ARD for Isothermal Calorimetry Experiments. The procedure used for making metal-free ARD (apoprotein) followed the same protocol described above for preparing reconstituted FeARD′ from expression and induction up to the point of dimethylglyoxime addition. Instead of dimethylglyoxime, sodium EDTA (pH 7.4) was added to the urea/DTT solution containing the unfolded ARD to a final EDTA concentration

of 10 mM. After stirring under Ar for 10 min, the solution was diluted 8-fold with degassed and Ar-saturated 50 mM Tris HCl/10 mM EDTA (pH 7.4). The dilution was stirred under Ar for 15 min, and insoluble material was removed by centrifugation (4000 × *g*, 1 h). The clarified supernatant was loaded onto a DEAE ion exchange column pre-equilibrated with 20 mM Tris, 10 mM EDTA, pH 7.4 (buffer A). After removal of unbound proteins with a 100 mL wash with buffer A, a linear gradient of 0−0.5 M NaCl in buffer A over a total volume of 250 mL was applied to the DEAE column, with the ARD-containing fractions identified by SDS−PAGE gel electrophoresis. These fractions were combined, concentrated, and applied to a S-200 size exclusion column pre-equilibrated with buffer A on an AKTA FPLC system. After elution as detected by UV detection (256 nm), the apoprotein was concentrated and dialyzed against 1 L of 50 mM MOPS, 10 mM EDTA (pH 7.0) for 12 h, with one buffer change at the 6-h point. EDTA was then removed by dialysis against 50 mM MOPS (pH 7.0) for 36 h with buffer changes every 6 h. Loss of protein was minimized by degassing of all dialysis buffers. The apoprotein was then concentrated appropriately for use in ITC experiments (see below).

Isothermal Calorimetry (ITC) Titrations for Metal Binding to WT, H98S, and E100A Mutant ARD Enzymes. In preparation for ITC experiments, all glassware was washed with 0.5 M HCl followed by 50 mM EDTA (sodium salt, pH 7.5) solution and extensive rinsing with MilliQ water. Nonsterile plastic ware was washed with 50 mM EDTA solution followed by extensive rinsing with MilliQ water. Sterile plastic ware was considered metal-free and used directly. A 1 M MOPS buffer (sodium salt, pH 7.0) stock solution was filtered and passed through a Chelex 100 resin column to remove trace metals. All subsequent working buffers were prepared by diluting this stock solution with Chelex-treated MilliQ water. Ultrapure $FeSO_4$ (99.999%) and $Ni(NO_3)_2$ (99.999%) were purchased from GFS Chemicals (Powell, OH). Metal stock solutions were prepared by dissolving the appropriate amount of salt (measured by weight of the solid) in 50 mM MOPS, pH 7.0. Since $FeSO_4$ is readily air-oxidized, the buffer was degassed for 1 h under vacuum and then purged with Ar for 45 min before solid $FeSO_4$ was added under an Ar atmosphere. All subsequent transfer steps for the Fe-containing buffers and samples for Fe titration were made in an Ar atmosphere. To prevent Fe^{2+} oxidation, 10 mM sodium dithionite was added to the $FeSO_4$ stock solution (*23*). Final concentrations for Ni and Fe stock solutions were 67 and 100 mM, respectively. All ITC experiments were performed using a MicroCal VP-ITC microcalorimeter at 25 °C (Boston Biomedical Research Institute, Watertown, MA). A Hastelloy C-276 sample cell was used for all experiments. ITC titrations were performed at 25 °C by injection of nanoliter amounts of the appropriate metal salt in MOPS buffer (pH 7.0) into solutions of apoprotein in the ITC cell. Appropriate protein concentrations were determined empirically to provide adequate signal-to-noise in the experiments. All ITC experiments reported were performed at least twice. Data analysis was performed using the Origin software provided with the MicroCal instrument.

XAS Methods. XAS data for resting state and substrate-bound FeARD′ were acquired at beamline X9B at the National Synchrotron Light Source (NSLS) at Brookhaven National Laboratory. Details of XAS data collection and analysis have been recently described for the resting state FeARD′ (*15*). Data collection for the ES complex was performed under identical conditions using a He cryostat to hold the sample temperature near 50 K. X-ray fluorescence data were collected using a 13-element Ge detector (Canberra). X-ray absorption data were collected over the range from ca. 6.9 to 8.1 KeV. Harmonic rejection was achieved by use of a Ni mirror. The average of 10 scans was used for EXAFS analysis by WinXAS (*24*). The coadded energy-calibrated datasets were corrected for background and normalized using two third-order polynomial fits. For XANES analysis, the pre-edge peak at ca. 7114 eV is associated with a 1s → 3d electronic transition. The area of the peak associated with this transition provides a reliable indication of coordination number and geometry and was determined by fitting a baseline to the pre-edge and edge regions of the spectra (ca. 7105−7120) using a cubic function for the pre-edge and 75% Gaussian and 25% Lorenzian function to fit the rise in fluorescence occurring at the edge, as previously described (see Supporting Information) (*25*). The difference between the fitted background and the spectrum was then integrated. The apparent edge energy of the samples was determined by finding the maximum in the first derivative of the XANES spectrum.

For EXAFS, the data were converted to *k* space using the expression $[2m_e(E - E_0)/\hbar^2]^{1/2}$, where m_e is electronic mass, E is the photon energy, $\hbar$ is Planck's constant divided by 2π, and E_0 is the threshold energy of the absorption edge, 7125.0 eV. A least-squares fit was employed over a range of $k = 2-12.5$ Å^{-1}. The fitting procedure minimized $1/\sigma^2 \sum_{i=1}^{N}[y_{exp}(i) - y_{theo}(i)]^2$, where σ is an estimate of the experimental error, y_{exp} and y_{theo} are experimental and theoretical data points, respectively, and N is the number of data points (*24*).

$$\text{residual[\]\%} = \left[\frac{\sum_{i=1}^{N}|y_{exp}(i) - y_{theo}(i)|}{\sum_{i=1}^{N}|y_{exp}(i)|}\right]100 \qquad (1)$$

Fits were generated to unfiltered data over the range of $k = 2-12.5$ Å^{-1} and were limited by noise in the data that was due largely to the dilute nature of the samples and the detector available. Theoretical phases and amplitudes for EXAFS analyses were obtained from calculations of model compounds catena-(hexakis(μ-2-imidazoyl-*N*,*N*′)bis(imidazole)tri-iron) (*26*) and $(Et_4N)_2[Fe(SC_6H_4CH_3\text{-}p)_4]$ using FEFF 8.2 (*27*). The EXAFS analysis of ES FeARD′ data was carried out as described previously (*28*). Integer values for the number of scattering atoms in a shell were used in the fits without further refinement. Fits were generated using three running parameters for each shell in the first coordination sphere including the distance (r), disorder (σ^2), and phase shift (ΔE_0). Comparison of the residual (eq 1) and the σ^2 parameter was used to select the best fits (*24*). The values of σ^2 in the best fits are about twice the value expected for a well-ordered shell of scattering atoms. This indicates that either the number of scattering atoms in the shell is too large or the site is disordered. Since the number of scattering atoms

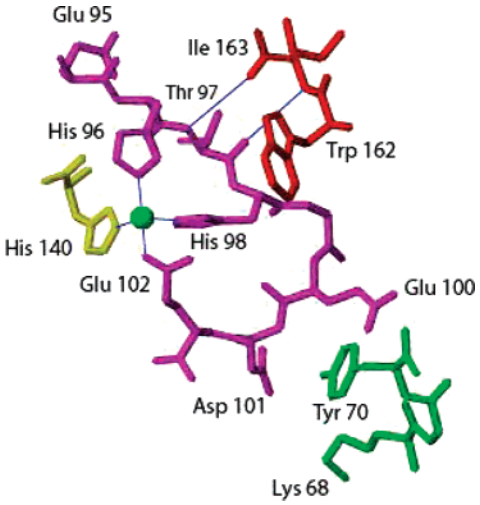

FIGURE 2: Details of the metal binding site in NiARD (PDB entry 1ZRR) emphasizing residues mutated in this study and discussed in the text. The nickel is shown as a green sphere. For clarity, the two equatorial water ligands that complete the Ni coordination are not shown. Backbone CO−NH hydrogen bonds between Thr97 and Ile163 and ligand−metal bonds are shown as thin blue lines. View is from the vantage point of the C-terminal end of the G helix (see Figure 1).

is determined by the XANES analysis to be six and since six scattering atoms in the EXAFS fits gave the best residual values, the best fits were selected from those fits containing six scattering atoms in the first coordination sphere (see Supporting Information). For each shell of scattering atoms in the first coordination sphere, three adjustable parameters were used (r, σ^2, and E_0). Histidine ligands were "counted" by substituting imidazole ligands for N/O-donor ligands in the first coordination sphere and using multiple scattering parameters to account for scattering from second coordination sphere C atoms and third coordination sphere C and N parameters, as previously described (*28*). The value of E_0 for C and N atoms in the imidazole ring was constrained to be the same as that for the first coordination sphere N-donor atom. This procedure estimates the number of histidine ligands to about ±25%, or about the same accuracy with which the number of scattering atoms in the first coordination sphere can be determined from EXAFS analysis alone. A table of selected fits and figures that illustrate the fit progression may be found in the Supporting Information.

RESULTS

Site-Directed Mutagenesis of Active Site Residues in ARD. X-to-Ala mutations were made for seven residues that either are expected to be metal ligands based on spatial proximity and strong sequence conservation (His96, His98, Glu102, and His140), have potential for metal ligation with minimal structural distortion (Glu100), or are conserved or show conservative replacement across the ARD family but are unlikely to provide metal ligands based upon structural considerations (Glu95, Asp101) (see Figure 2). In addition, mutations were made at His98 (H98S) and His140 (H140F) that preserve specific features of the wild-type (polarity at 98, side-chain planarity at 140). Properties of the mutant proteins are summarized in Table 1. Mutations at three of the proposed ligands, His96, Glu102, and His140, all result in decreased expression of soluble protein, with the H140A mutant giving no soluble protein. H140F, E102A, and H96A all produce some soluble protein, but the majority remains in the pellet after cell lysis.

Table 1: Characterization of ARD Mutants

mutation	% in cytosol[a]	specific activity (U)[b]	metal content as isolated[c]
WT	100	50[d]	
E95A	>70	1.8	Fe <0.002 Ni 0.02
H96A	<50	background	
H98A	>70	background	
H98S	100	background	Fe <0.002 Ni <0.01
E100A	100	0.8 (Ni-reconstituted)[e] 0.5 (Fe-reconstituted)[f]	Ni <0.01 Fe 0.17
D101A	>70	32 (as isolated)[g]	Ni 0.1 Fe 0.3
E102A	<50		
H140A	0		
H140F	<50		

[a] Approximate percent of protein in cytosol relative to total cytosol plus insoluble (pellet) after cell lysis, estimated by SDS−PAGE electrophoresis. [b] Activity estimated by loss of signal intensity of acireductone substrate peak under standard assay conditions in units U = micromoles of substrate per minute per milligram of enzyme. Specific activities are corrected for background rates of acireductone oxidation. [c] Metal contents are fractional contents, moles of metal per mole of protein, determined by graphite furnace atomic absorption spectrometry (GF-AAS) by Dr. Peter Kerr, University of Massachusetts, Amherst. [d] WT activity is for NiARD with CO production. [e] Ni reconstitution of E100A gives off-pathway activity with CO production. [f] Fe reconstitution of E100A gives on-pathway activity with keto-acid production. [g] D101A as isolated has on-pathway activity (keto-acid production); off-pathway activity is unconfirmed.

Table 2: Isothermal Calorimetry Results for apo-WT, E100A, and H98S ARD[a]

mutation	K_d(app), Ni^{2+} [N]	protein concn (μM) Ni titration	K_d (app), Fe^{+2} [N]	protein concn (μM) Fe titration
WT	≤0.1 μM [0.8]	5	≤0.4 μM [0.5]	25
H98S	>50 μM	50	>50 μM	50
E100A	≤0.2 μM [0.8]	10	≤0.2 μM [0.6]	50

[a] All experimental data sets were best fit to a one-site model, and all experiments were repeated at least twice. [N] is the stoichiometry ratio (moles of metal/moles of protein) yielding the apparent K_d. Apparent K_d values represent upper limits to actual dissociation constants.

Mutations at the fourth protein-based ligand, His98, were of particular interest. The H98A mutant produces a greater fraction of soluble protein than the other three ligand-to-alanine mutants (H140A, H96A, and E102A), and the H98S mutant is, like WT, expressed only as soluble protein. We noted that the H98S mutation is isostructural with FeARD′ based upon comparison of multidimensional NMR data, and the structure of H98S ARD was used along with FeARD′ XAS data to determine a model for the structure of FeARD′ by NMR methods (*15*). However, H98S ARD exhibits little affinity for either Ni^{2+} or Fe^{2+} as measured by ITC titration (see Table 2) indicating that His98 is likely involved in binding both metals.

The other residue considered as a potential "switch" ligand was Glu100. Assuming alternating β-sheet arrangement of amino acid side chains, the side chain of Glu100 is in register

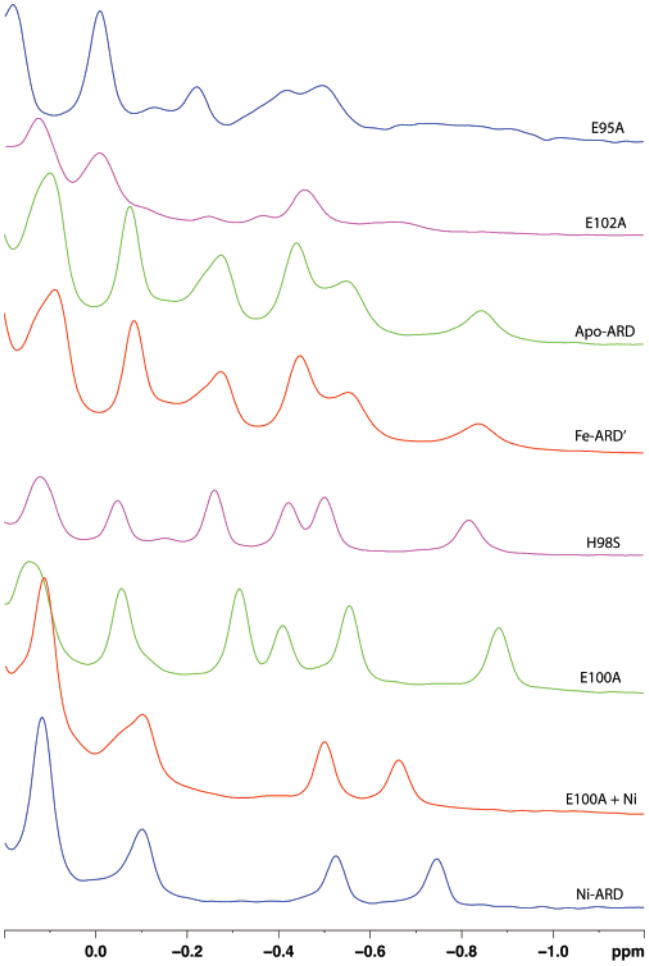

FIGURE 3: Comparison of the upfield region of the ^{1}H NMR spectra of various ARD mutants and isoforms. Spectra are arranged so that similarities are emphasized. From top to bottom, E95A as isolated (purple), E102A (carmine), apo-WT ARD (green), FeARD′ (red), H98S (carmine), E100A as isolated (green), E100A reconstituted with Ni^{2+} (red), and NiARD (purple). All resonances in this region are due to methyl groups in close-packing arrangements with aromatic side chains (*15*). Note that both E95A and E102A show fewer resonances in this region, indicating a lower degree of order in their structures. ApoARD and FeARD′ have very similar folds, as does H98S (*15*). Apo-E100A shows some similarity to H98S, but after reconstitution with Ni^{2+} shows a high degree of similarity with NiARD. Detailed resonance assignments of H98S and NiARD are available from the BMRB database (www.bmrb.wisc.edu), accession numbers 7103 and 4313, respectively.

with His96, His98, and Glu102 and like His98 is also part of the loop between the two outermost strands of the β-sandwich. With relatively little distortion of the polypeptide, it might be possible for Glu100 to either ligate metal ion as a fifth protein-based ligand or act as a replacement for His98 in one or the other isoform. The E100A mutant is expressed primarily as soluble protein, with an upfield ^{1}H NMR spectrum reminiscent of H98S and FeARD′ (Figure 3), which we have identified as the "default" fold for the ARD polypeptide (*15*). The E100A mutant has high affinity for both Ni^{2+} and Fe^{2+} as determined by ITC experiments, on the same order of magnitude as WT (Table 2), indicating that Glu100 is not an essential ligand for either metal ion. However, the activities of both the Fe- and Ni-reconstituted E100A mutant are considerably lower than WT enzyme, suggesting that Glu100 is involved in some manner in enzyme function.

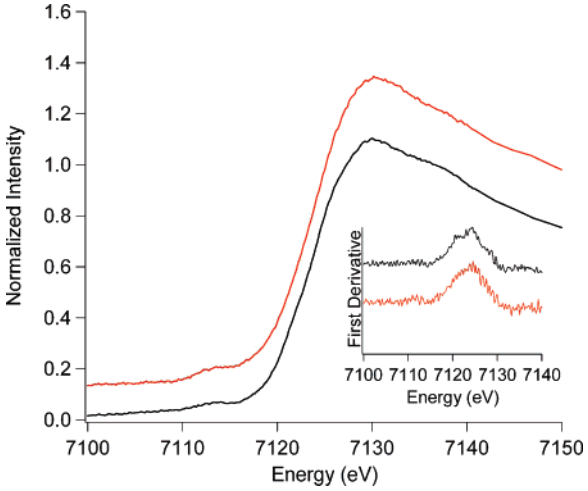

FIGURE 4: Fe *K*-edge XANES of the resting state (black) and ES complex (red, offset) of FeARD′. The region around 7114 eV corresponds to the 1s → 3d transition. The inset shows the first derivative of the XANES in the edge region.

Neither Glu95 or Asp101 are expected to ligate the active site metal, since both have their side chains external to the β-sandwich. However, Glu95 is strictly conserved in known ARD sequences, and somewhat surprisingly, E95A is expressed primarily as soluble apoprotein (Table 1), with background amounts of Fe present and ~2% Ni incorporation. Based on the upfield region of the ^{1}H NMR spectrum the E95A mutant exhibits a perturbed structure resembling that of E102A (Figure 3). As isolated, E95A shows slight activity above background, but this could be due to the presence of a small amount of active Ni-containing protein.

The upfield ^{1}H spectrum of D101A is complex (data not shown), suggesting multiple forms are present. The D101A mutant as isolated contains significant amounts of both Ni and Fe. However unlike WT ARD, we could not separate distinct Ni- and Fe-containing fractions using either ion-exchange or hydrophobic interaction chromatography. D101A is also the only mutant described here that exhibits significant activity (Table 1) as isolated. While we have not confirmed carbon monoxide production by this mutant, we see α-keto-acid formation consistent with ARD′ activity.

XANES Analysis. The XANES spectra for resting FeARD′ and the FeARD′ ES complex are compared in Figure 4. The edge energies determined as the maximum in the first derivative spectrum are 7123.8(2) eV for the resting enzyme and 7124.0(2) eV for the ES complex. There is no significant difference in edge energy observed between the resting form and ES complex of FeARD, indicating that no redox change occurs upon substrate binding, as a one-electron metal-centered redox reaction is expected to result in a 2−3 eV shift (*25*).

At energies near 7113 eV, a peak corresponding to a process involving a 1s → 3d electronic transition is observed. The area under this peak has been shown to be a good measure of the coordination number and geometry in a number of crystallographically characterized iron complexes (*29*). The peak areas determined for the resting FeARD′ and the ES complex are $5.8(1) \times 10^{-2}$ eV and $6.9(7) \times 10^{-2}$ eV, respectively, and indicate that the complexes are six coordinate in both cases (*29*−*31*).

EXAFS Analysis. The EXAFS unfiltered and Fourier-transformed spectra for resting FeARD′ and the FeARD′ ES

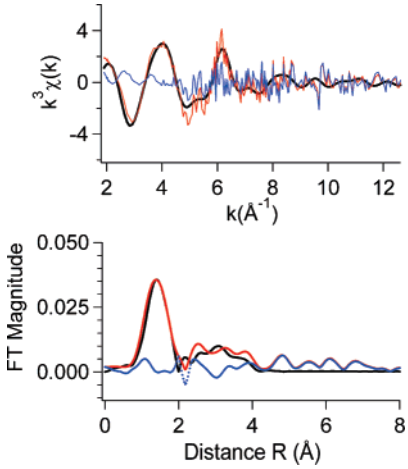

FIGURE 5: Fe *K*-edge (k = 2−12.5 Å^{-1}) EXAFS spectrum for resting FeARD′: top, k^3-weighted spectrum (red line), fit (black line), and difference (data-fit; blue line); bottom, Fourier-transformed data, fit, and difference. The fit shown was calculated for two O at 2.15 Å and four N at 1.98 Å, including three histidine ligands and corresponds to fit R13 in the supplementary table.

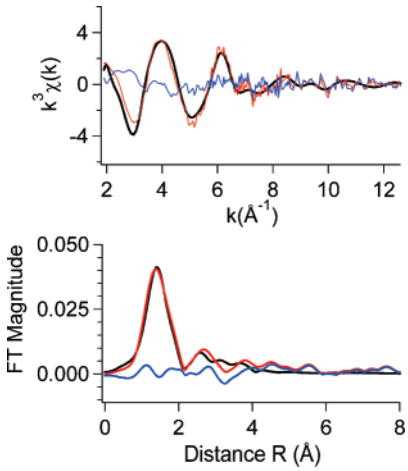

FIGURE 6: Fe *K*-edge (k = 2−12.5 Å^{-1}) EXAFS spectrum for FeARD′ ES complex: top, k^3-weighted spectrum (red line), fit (black line), and difference (data-fit; blue line); bottom, Fourier-transformed data, fit, and difference. The fit shown was calculated for three O at 2.15 Å and three N at 1.98 Å including one histidine ligand and corresponds to fit ES08 in the supplementary table.

complex are compared in Figures 5 and 6, respectively. Visual inspection of the data indicates a change in the spectrum when substrate is added, implying that the substrate binds to the Fe site. One change that occurs is a decrease in the intensity of features in the Fourier-transformed spectrum at a radial distance of ca. 3−4 Å (uncorrected for phase shifts) in the spectrum of ES complex. These features are generally attributed to the presence of histidine imidazole ligands; thus, inspection of the spectra indicates either the displacement of a histidine ligand or that a large increase in static disorder leading to an increase of σ^2 occurs upon substrate binding. The curve-fitting analyses of the EXAFS data presented are more consistent with the loss of a histidine ligand upon substrate binding, since the values of σ^2 observed for the first coordination sphere scattering atoms are generally lower (more ordered) in the ES complex, and generally support the qualitative results and provide metric details regarding the Fe sites (see Supporting Information).

The EXAFS data obtained from resting FeARD′ are consistent with a six-coordinate Fe site composed exclusively of O/N-donor ligands; inclusion of a S-donor ligand leads to poorer fits relative to fits employing O/N-donors (see Supporting Information). However, as noted in the Materials and Methods section (*vide supra*) relatively low signal-to-noise in acquisition and the likelihood of static disorder in the FeARD′ active site (as gauged by metal−ligand bond lengths from the crystallographic structure of the *Mm*ARD (17)) makes it difficult to clearly identify a single "best-fit" combination of N/O donors and metal-scatterer distances. Comparable fits were obtained with either O- or N-donors and when the ΔE_0 was constrained to a single value for fitting both first and second + third shell scattering atoms or was allowed to vary by atom type (N vs O) and shell. The best fit of the data obtained using one value of E_0 for N-donors (imidazole ligands) and one E_0 for other first coordination sphere donors (O-donors) featured two (N)O-donor ligands at an average distance of ∼1.90 Å and four N(O)-donor ligands with an average distance of ∼2.06 Å, of which three are consistent with histidine imidazole side chains when second and third coordination sphere atoms are included: $Fe(His)_3(N/O)_3$ (Figure 5, see Supporting Information).

The ligand environment of the Fe center in the ES complex is also best fit by a combination of six N/O-donor ligands. In this case, the fit is consistent with three (N)O-donor ligands at an average distance of ∼1.92 Å and three N(O)-donors at an average distance ∼2.15 Å, of which one of the ligands is a histidine imidazole side chain: $Fe(His)_1(N/O)_5$ (Figure 6, see Supporting Information). Fits were not improved by including a S-donor. The presence of histidine N-donor ligands in the FeARD′ ES complex is confirmed by multiple scattering analysis. Modeling one of the first coordination sphere N-donor ligands as a histidine imidazole ligand leads to improvements in the residuals of the fits. However, in this case it is difficult to distinguish whether one or two imidazole ligands are bound.

The crystallographic structure of *Mm*ARD shows the metal (presumed but not proven to be Ni^{2+}) bound by a three-histidine one-glutamate ligation scheme, identical in geometry and sequentially homologous to that proposed in the NMR-derived structures of both NiARD and FeARD′ (*13*, *17*). The metal−N distances for the three histidine ligands are 2.02 Å (His133), 2.05 Å (His90), 2.19 Å (His88) and the metal−carboxylate O distance (Glu94) is 2.2 Å. The two remaining sites in the octahedral ligation sphere of the metal not occupied by protein-based ligands are *cis* to each other in equatorial positions and are occupied by an unidentified molecule(s) with N/O ligand distances to the metal of 2.17 Å and 2.25 Å. The ligation geometry of the metal is distorted octahedral, with N−Me−N bond angles averaging 97.9° and those between the unknown ligand (L) and the carboxylate L−Me−O averaging 85.5°. The L−Me−L angle between substrate atoms is 72°, and the angle between the ligand carboxylate O of Glu94 and the adjacent histidine N ligand (His90) is 81°. The >0.2 Å spread in M−N/O distances (2.02−2.25) observed in this structure indicates a high degree of static disorder in the M−L distances and accounts in part for the larger than typical values of σ^2 in the EXAFS models, which were constrained to a maximum of two shells in the first coordination sphere in order to minimize the number of free running parameters in the fits and still accommodate both N- and O-scattering atoms.

Isothermal Calorimetry Titrations of WT, H98S, and E100A ARD. Isothermal calorimetry experiments were performed to measure binding of metal ions to three metal-free ARD proteins, WT, E100A, and H98S (Table 2). We note that these experiments can only provide an upper limit for K_d for metal binding because in order to obtain a detectable signal, a minimum of 5 μM protein (in the best case, that of WT) is required, putting the upper limit for accuracy in calculating K_d at best at 0.05 μM. Somewhat higher protein concentrations were required for E100A titrations in order to obtain clean isotherms, but strong binding of both Fe^{2+} and Ni^{2+} were observed with this mutant. On the other hand, a minimum of 50 μM H98S mutant was required in order to detect any heat release above background upon addition of Ni^{2+}, and no reasonable fit could be made to the data. No heat release was observed above background for binding of Fe^{2+} to H98S, even at 50 μM protein. Furthermore, even when binding of Fe^{2+} was clearly detected (in the cases of WT and E100A), best fits of binding isotherms gave half-of-the-sites stoichiometry as saturating Fe^{2+} concentrations, suggesting that Fe^{2+} binding may drive a dimerization event under the conditions of the ITC experiment (although no evidence for dimerization is observed either by NMR or by size-exclusion chromatography for WT FeARD′ folded *in vivo* or by reconstitution for XAS as described above). For these reasons, ITC performed by direct titration does not provide accurate measures for metal binding affinities, and no direct comparison between Fe^{2+} and Ni^{2+} binding affinities is possible using the present data. Still, ITC data provides strong evidence for the conclusion that while His98 is essential to binding both Fe^{2+} and Ni^{2+}, Glu100 is not essential in either case.

DISCUSSION

The four residues that we have identified as ligating the active site metal in both FeARD′ and NiARD isoforms, His96, His98, Asp102, and His140, are all strictly conserved across the ARD superfamily (*31*) and were initially identified as potential ligands via sequence alignment and spatial localization from paramagnetic broadening patterns in NMR data and homology modeling (*12*). The recently published crystal structure of *Mm*ARD supports the assignment of these residues as the protein-based ligands (*17*). However, the identity of the metal in the *Mm*ARD structure is unknown, and considering the importance of the identity of the metal in determining both structure and function of ARD, the possibility of alternate metal binding modes involving ligand switching between FeARD′ and NiARD could not be ignored. Our primary suspect in this regard was His98. Unlike His96, Glu102, and His140, which all reside in well-defined β-structure, His98 is found on a potentially flexible loop between two strands and is adjacent to a glycine residue, Gly99. As such, His98 seemed the most likely of the four to act as a structural switch between FeARD′ and NiARD binding. However, ITC and spectroscopic studies indicate that the H98S mutant does not bind either metal strongly, indicating that His98 is a ligand for both Fe^{2+} and Ni^{2+}.

Besides the three-histidine one-glutamate ligand tetrad, a number of other acidic residues in the active site region of ARD are either also strictly conserved (Glu95) or conservatively substituted (aspartate for Glu100, glutamate for Asp101) across the superfamily (*32*). Of particular interest in this regard is Glu100. Based on the even registry of the three ligands (His96, His98, Glu102) and its position on the inter-strand loop (Thr97-His98-Gly99-Glu100-Asp101), Glu100 appeared to be structurally well-placed to either provide an extra ligand to the metal with little structural distortion or replace a ligand in one or the other isoform. However, ITC data shows that the E100A mutant binds both Ni^{2+} and Fe^{2+} readily, and the ^{1}H NMR fingerprint of Ni-reconstituted E100A ARD is remarkably similar to that of WT NiARD (Figure 3). Furthermore, the Ni-reconstituted E100A ARD shows CO production from acireductone under standard assay conditions, with no significant α-keto-acid production, indicating NiARD activity, while the Fe-reconstituted form gives rise to α-keto-acid, indicating FeARD′-like activity. As such, we conclude that Glu100 is not an essential metal ligand in either ARD isoform. However, we also note that the activities of both reconstituted forms of E100A ARD were much lower than WT (while still maintaining the same metal-dependent chemoselectivity as WT). It is clear that Glu100 plays a role in the chemistry catalyzed by ARD in both isoforms, and we are currently investigating this function in more detail.

Finally, the roles of the strictly conserved Glu95 and conservatively substituted Asp101 must be considered. Neither residue is suitable for direct metal ligation. In all three ARD structures, the carboxylate side chain of Glu95 (Glu87 in *Mm*ARD) is surface-exposed, and its orientation is fixed by the register of the β-helix. In NiARD, the carboxylate of Glu95 is positioned to interact with portions of the C-terminal peptide (Gly168−Asp170) that precedes the C-terminal 3,10-helix (*13*). In *Mm*ARD, the homologous Glu87 forms a surface salt bridge with a nonconserved arginine, Arg108. The fact that the E95A mutant is isolated primarily as apoprotein and shows a distorted structure similar to that of a ligand mutant (Figure 3) suggests that Glu95 plays a role in metal incorporation *in vivo*, either by stabilizing the structure of the active site in the apoprotein or assisting in metal transfer from a metallochaperone.

The D101A mutant incorporates metal *in vivo* and shows the highest enzymatic activity of any of the mutants described here. Structurally, the carboxylate of Asp101 (conservatively replaced by Glu93 in *Mm*ARD) interacts with a conserved tyrosine (Tyr70 in ARD, Tyr61 in *Mm*ARD) and a conserved positively charged residue at the C-terminus of the E′ helix (Lys68, Arg59 in *Mm*ARD). This region has been implicated in the structural switch between NiARD and FeARD′ (*15*). In NiARD, this region is structurally well-defined and is important in determining the formation of secondary structure in the turn-loop that directs the packing of the C-terminal 3,10 helix onto the top of the β-sandwich as viewed in Figure 1. In FeARD′, this region occupies multiple conformations on the NMR time scale, and the C-terminal end is disordered. This disorder, as well as the repacking of the E,E′ helices against the bottom of the β-sandwich, has been identified as key structural differences between NiARD and FeARD′ and results in a more open active site for ARD′ than for ARD (*15*). Based on the current results, we propose that Asp101 plays an important role in transmitting local conformational changes in the ARD active site that occur upon Ni binding to other parts of the protein. Current experiments are aimed at clarifying that role.

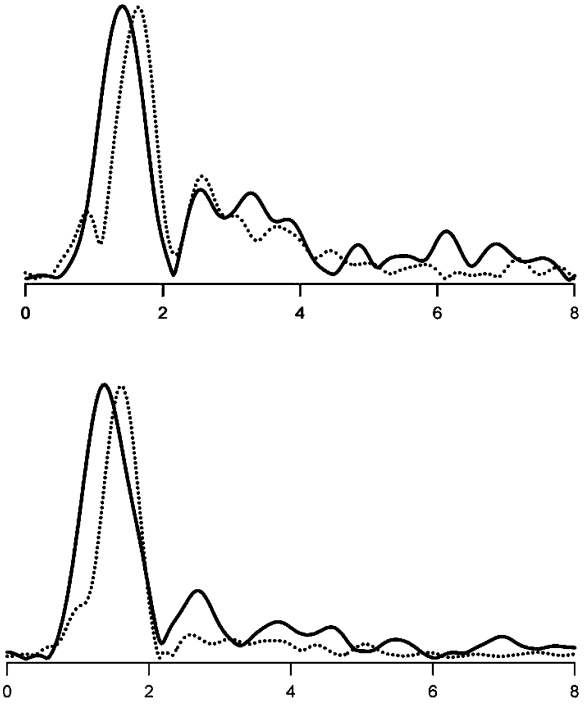

FIGURE 7: Comparison of the Fe *K*-edge Fourier-transformed EXAFS spectra ($k - 2-12.5$ Å^{-1}) of FeARD′ (solid) and Ni *K*-edge EXAFS spectra of NiARD (dashed) of the resting state (top) and ES complex (bottom) from *Klebsiella* ATCC 8724.

Comparison of the FeARD′ and NiARD Resting State and ES Complexes by XAS. Despite the difficulty in obtaining a clear best-fit solution to the EXAFS data, the XAS results allow us to conclude that the structures of the Fe centers in resting FeARD′ and in the FeARD′ ES complex are strikingly similar to those in the corresponding Ni centers in NiARD and NiARD ES complex (*14*). The Ni center in resting NiARD was found to be six coordinate with exclusively N/O ligation including three to four histidine imidazole donors: $Ni(His)_{3-4}(O/N)_{2-3}$ with one O-donor at 1.91 Å and five N/O donors at 2.10 Å. Acireductone was shown to bind to NiARD with the apparent displacement of a histidine, and the predicted NiARD ES complex consists of four O-donors at a Ni−O distance of 2.00 Å and two N-donors at 2.14 Å, with one or two of the ligands being provided by a histidine: $Ni(His)_{1-2}(O/N)_{4-5}$. The XAS data thus appear to rule out a change in the type and number of ligand donors or coordination geometry and do not support the idea that Fe and Ni are coordinated to different ligands in the two enzymes. Figure 7 compares the Fourier-transformed spectra for FeARD′ and NiARD in the resting state and ES complex. The spectra for both ARD proteins are scaled so that the major peaks at a radial distance ~2 Å in both spectra have comparable intensities. Both spectra show common features and are consistent with the binding of the metal ion to the same ligand set in both FeARD′ and NiARD. These results are completely consistent with the results from mutagenesis and ITC experiments, both of which support the hypothesis that the same ligand set binds metal in the resting states of NiARD and FeARD′. Furthermore, the data are also consistent with the formation of similar ES complexes for both isoforms.

In the absence of different ligand sets for the two isoforms, we considered the possibility that the different chemistries of NiARD and FeARD′ are due to different redox activities of the bound metals. However, nickel in a N/O-donor ligand environment is not expected to have a biologically accessible redox potential (*33*). Replacement of Ni^{2+} by Fe^{2+} could give rise to a mechanism involving activation of O_2. However, metal replacement experiments show that FeARD′ activity can be partially reconstituted in apo-ARD by addition of Mg^{2+}, another non-redox-active metal ion (*12*). As such, it appears unlikely that the activity differences between the isoforms arise from differences in redox potential. No EPR signal has been observed for FeARD′ under aerobic/anaerobic conditions in the presence or absence of acireductone, consistent a divalent Fe center (*20*), and this oxidation state is supported by the Fe K-edge energies observed for both the FeARD′ and the FeARD′ ES complex.

Implications for Structural and Reactivity Differences. A central question still remains: If both the resting state and ES complexes of FeARD′ and NiARD have the same overall geometry, and differences in redox chemistry do not enter into consideration, how do binding of Fe and Ni give rise to different protein structures and different products from the same substrates? We have proposed that relatively small differences between the two metal binding modes could be amplified via a contraction of the ligation sphere around Ni^{2+} relative to Fe^{2+} or a switch between N_δ and N_ϵ ligation at His98 (*15*) or both. Either or both differences could be sufficient to trigger a conformational change in the Thr97-His98-Gly99-Glu100-Asp101 interstrand loop, which in turn could result in the more widespread changes that are observed in the switch between NiARD and FeARD′. Intermediate in the proposed trigger is an antiparallel hydrogen bonding arrangement involving the backbone NHs and carbonyl oxygens of Thr97 and Ile163 in the NiARD structure that is inferred from the *Mm*ARD crystal structure (Figure 2) (*13*). This interaction is clearly missing in the FeARD′ structure, as is the salt bridge/polar interactions involving Lys68, Tyr70, and Asp101 discussed above. The Thr97−Ile163 backbone hydrogen bond appears to be critical for stabilizing the structure of the O turn-loop and the P C-terminal helix in NiARD (Figure 1). The Asp101-Lys68-Tyr70 interaction also likely contributes to stabilizing this structure, as the loop region from Lys68 to residue 71 following the C-terminal of helix E′ is disordered in FeARD′ (*15*). The net effect of these differences is to restrict access to the active site in NiARD via side chains that project from loop O near the metal cluster, particularly the indole of Trp162. We have proposed a mechanism to account for the different chemistries catalyzed by NiARD and FeARD′ based on alternative modes of metal−substrate ligation resulting in Lewis acid activation of either C-2 (in FeARD′) or C-3 (in NiARD) toward intramoleuclar nucleophilic attack by peroxide anion (*12*, *13*).

The XAS data presented here provide the first detailed structural information regarding Fe binding in the FeARD′ ES complex and help to establish key early steps in reaction mechanism. Because both the resting enzyme and the FeARD′ ES complex contain six-coordinate Fe centers, binding acireductone as a bidentate ligand would require the substitution of two ligands from the Fe center in the resting enzyme. Although we have previously modeled this interaction as resulting from the displacement of the two solvent-derived ligands, comparison of the EXAFS data for the resting FeARD′ and the ES complex suggests that at least

one of these displaced ligands is a histidine. A similar situation is observed in the case of NiARD (*14*).

Another interesting result of the current work is that even mutations at residues not directly involved in metal ligation (Glu95 and Glu100) appear to hamper metal incorporation *in vivo* (see Table 1). This is particularly obvious from the E100A mutant. While this mutant readily bound both Fe^{2+} and Ni^{2+} *in vitro* with exothermicity comparable to WT, the protein was isolated primarily as apoprotein, with very low nickel content and less than 20% of the Fe-bound form. This leads us to speculate that the conserved acidic residues in ARD play a role in metal incorporation via transfer from metallochaperones (*34*). The upfield methyl "fingerprint" of the ^{1}H NMR spectrum is exquisitely sensitive to changes in packing of hydrophobic residues in ARD. Comparisons between NiARD, FeARD′, and H98S (*15*) show that differences in this spectral region are primarily due to perturbations in the packing of the E and E′ helices against the bottom of the β-sandwich, which in turn appears to be driven by changes in the vicinity of the active site. It is possible that metal binding by some or all of these residues during folding provides a template around which the active site can properly form and that in their absence, incorrect forms can accumulate. Certainly, the polypeptide in the vicinity of the ARD active site must be exquisitely sensitive to environment. Even using the same set of ligands, differences in Fe and Ni binding are sufficient to initiate dramatic structural changes that propagate through much of the molecule external to the β-sandwich.

ACKNOWLEDGMENT

The authors thank Dr. Lingyun Rui for help in setting up the CO assay, Dr. Knut Langsetmo (Boston Biomedical Research Institute) for access to their ITC instrument and his generous help in training, Prof. Susan Sondej Pochapsky for help with figures, Ms. Becky Myers for sequencing work, and Prof. Lisbeth Hedstrom for helpful discussions.

SUPPORTING INFORMATION AVAILABLE

Fits for resting state and ES complex EXAFS data, fit progressions, and peak area background corrections. This material is available free of charge via the Internet at http://pubs.acs.org.

REFERENCES

1. Schlenk, F. (1983) Methylthioadenosine, *Adv. Enzymol. 54*, 195−265.
2. Oredsson, S. M. (2003) Polyamine dependence of normal cell-cycle progression, *Biochem. Soc. Trans. 31*, 366−370.
3. Marton, L. J., and Pegg, A. E. (1995) Polyamines as targets for therapeutic intervention, *Annu. Rev. Pharmacol. Toxicol. 35*, 55−91.
4. Pegg, A. E. (1988) Polyamine metabolism and its importance in neoplastic growth and as a target for chemotherapy, *Cancer Res. 48*, 759−774.
5. Shapiro, S. K., and Barrett, A. (1981) 5-Methylthioribose as a precursor of the carbon chain of methionine, *Biochem. Biophys. Res. Commun. 102*, 302−307.
6. Wray, J. W., and Abeles, R. H. (1995) The methionine salvage pathway in *Klebsiella pneumoniae* and rat liver. Identification and characterization of two novel dioxygenases, *J. Biol. Chem. 270*, 3147−3153.
7. Dai, Y., Wensink, P. C., and Abeles, R. H. (1999) One protein, two enzymes, *J. Biol. Chem. 274*, 1193−1195.
8. Myers, R. W., Wray, J. W., Fish, S., and Abeles, R. H. (1993) Purification and characterization of an enzyme involved in oxidative carbon-carbon bond cleavage reactions in the methionine salvage pathway of *Klebsiella pneumoniae*, *J. Biol. Chem. 268*, 24785−24791.
9. Sekowska, A., Denervaud, V., Ashida, H., Michoud, K., Haas, D., Yokota, A., and Danchin, A. (2004) Bacterial variations on the methionine salvage pathway, *BMC Microbiol. 4*.
10. Wray, J. W., and Abeles, R. H. (1993) A bacterial enzyme that catalyzes formation of carbon monoxide, *J. Biol. Chem. 268*, 21466−21469.
11. Dunwell, J. M., Purvis, A., and Khuri, S. (2004) Cupins: the most functionally diverse protein superfamily? *Phytochemistry 65*, 7−17.
12. Pochapsky, T. C., Pochapsky, S. S., Ju, T., Mo, H. P., Al-Mjeni, F., and Maroney, M. J. (2002) Modeling and experiment yields the structure of acireductone dioxygenase from *Klebsiella pneumoniae*, *Nat. Struct. Biol. 9*, 966−972.
13. Pochapsky, T. C., Pochapsky, S. S., Ju, T., Hoefler, C., and Liang, J. (2006) A refined model for the structure of acireductone dioxygenase from *Klebsiella* ATCC 8724 incorporating residual dipolar couplings, *J. Biomol. NMR 34*, 117−127.
14. Al-Mjeni, F., Ju, T., Pochapsky, T. C., and Maroney, M. J. (2002) XAS investigation of the structure and function of Ni in acireductone dioxygenase, *Biochemistry 41*, 6761−6769.
15. Ju, T., Goldsmith, R. B., Chai, S. C., Maroney, M. J., Pochapsky, S. S., and Pochapsky, T. C. (2006) One protein, two enzymes revisited: A structural entropy switch interconverts the two isoforms of acireductone dioxygenase, *J. Mol. Biol. 363*, 523−534.
16. Ko, T. P., Day, J., and Mcpherson, A. (2000) The refined structure of canavalin from jack bean in two crystal forms at 2.1 and 2.0 Angstrom resolution, *Acta Crystallogr. D56*, 411−420.
17. Xu, Q., Schwarzenbacher, R., Sri Krishna, S., McMullan, D., Agarwalla, S., Quijano, K., Abdubek, P., Ambing, E., Axelrod, H., Biorac, T., Canaves, J. M., Chiu, H.-J., Elsliger, M.-A., Grittini, C., Grzechnik, S. K., DiDonato, M., Hale, J., Hampton, E., Han, G. W., Haugen, J., Hornsby, H., Jaroszewski, L., Klock, H. E., Knuth, M. W., Koesema, E., Kreusch, A., Kuhn, P., Miller, M. D., Moy, K., Nigoghossian, E., Paulsen, J., Reyes, R., Rife, C., Spraggon, G., Stevens, R. C., van den Bedem, H., Velasquez, J., White, A., Wolf, G., Hodgson, K. O., Wooley, J., Deacon, A. M., Gogzik, A., Lesley, S. A., Wilson, I. A. (2005) Crystal structure of acireductone dioxygenase (ARD) from Mus musculus at 2.06 Å resolution, *Proteins: Struct., Funct. Genet. 64*, 808−813.
18. Hirano, W., Gotoh, I., Uekita, T., and Seiki, M. (2005) Membrane-type 1 matrix metalloproteinase cytoplasmic tail binding protein-1 (MTCBP-1) acts as an eukaryotic aci-reductone dioxygenase (ARD) in the methionine salvage pathway, *Genes Cells 10*, 565−574.
19. Dai, Y., Wensink, P. C., and Abeles, R. H. (1999) One protein, two enzymes, *J. Biol. Chem. 274*, 1193−1195.
20. Dai, Y., Pochapsky, T. C., and Abeles, R. H. (2001) Mechanistic studies of two dioxygenases in the methionine salvage pathway of *Klebsiella pneumoniae*, *Biochemistry 40*, 6379−6387.
21. Sundin, A. M., and Larsson, J. E. (2002) Rapid and sensitive method for the analysis of carbon monoxide in blood using gas chromatography with flame ionisation detection, *J. Chromatogr. B 766*, 115−121.
22. Zhang, Y. L., Heinsen, M. H., Kostic, M., Pagani, G. M., Riera, T. V., Perovic, I., Hedstrom, L., Snider, B. B., and Pochapsky, T. C. (2004) Analogs of 1-phosphonooxy-2,2-dihydroxy-3-oxo-5-(methylthio)-pentane, an acyclic intermediate in the methionine salvage pathway: a new preparation and characterization of activity with E1 enolase/phosphatase from *Klebsiella oxytoca*, *Bioorg. Med. Chem. 12*, 3847−3855.
23. Bou-Abdallah, F., Arosio, P., Santambrogio, P., Yang, X., Janus-Chandler, C., and Chasteen, N. D. (2002) Ferrous ion binding to recombinant human H-chain ferritin. An isothermal titration calorimetry study, *Biochemistry 41*, 11184−11191.
24. Ressler, T. (1997) WinXAS: A new software package not only for the analysis of energy-dispersive XAS data, *J. Phys. IV 7*, 269−270.
25. Colpas, J. G., Maroney, M. J., Bagyinka, C., Kumar, M., Willis, W. S., Suib, S. L., and Mascharak, P. (1991) P.K. X-ray spectroscopic studies of nickel complexes, with application to the structure of Ni sites in hydrogenases, *Inorg. Chem. 30*, 920−928.

26. Lehnert, R., and Seel, F. (1978) Crystal structure of iron(II) derivative of imidazole, *Z. Anorg. Allg. Chem. 444*, 91−96.
27. Kang, B., and Cai, J. (1985) Formation and crystal structure of $(Et_4N)_2[Fe(SC_6H_4CH_3\text{-}p)_4]$, *Jiegou Huaxue 4*, 119−122.
28. Davidson, G., Clugston, S. L., Honek, J. F., and Maroney, M. J. (2001) An XAS investigation of product and inhibitor complexes of Ni-containing GlxI from *Escherichia coli*: Mechanistic implications, *Biochemistry 40*, 4569−4582.
29. Roe, A. L., Schneider, D. J., Mayer, R. J., Pyrz, J. W., Widom, J., and Que, L. (1984) X-Ray absorption spectroscopy of iron-tyrosinate proteins, *J. Am. Chem. Soc. 106*, 1676−1681.
30. Randall, C. R., Zang, Y., True, A. E., Que, L., Charnock, J. M., Garner, C. D., Fujishima, Y., Schofield, C. J., and Baldwin, J. E. (1993) X-ray absorption studies of the ferrous active site of isopenicillin N-synthase and related model complexes, *Biochemistry 32*, 6664−6673.
31. Bertini, I., Briganti, F., Mangani, S., Nolting, H. F., and Scozzafava, A. (1994) X-Ray absorption studies on catechol 2,3-dioxygenase from *Pseudomonas putida* Mt2, *Biochemistry 33*, 10777−10784.
32. Sauter, M., Lorbiecke, R., OuYang, B., Pochapsky, T. C., and Rzewuski, G. (2005) The immediate-early ethylene response gene OsARD1 encodes an acireductone dioxygenase involved in recycling of the ethylene precursor S-adenosylmethionine, *Plant J. 44*, 718−729.
33. Maroney, M. J. (1999) Structure/function relationships in nickel metallobiochemistry, *Curr. Opin. Chem. Biol. 3*, 188−199.
34. Dosanjh, N. S., and Michel, S. L. J. (2006) Microbial nickel metalloregulation: NikRs for nickel ions, *Curr. Opin. Chem. Biol. 10*, 123−130.
35. Kraulis, P. J. (1991) Molscript - a program to produce both detailed and schematic plots of protein structures, *J. Appl. Crystallogr. 24*, 946−950.

BI7004152